Maintenance of the Zonal Momentum Balance of the Antarctic Circumpolar Current by Barotropic Dynamics

XIHAN ZHANG,[a,b,c] MAXIM NIKURASHIN,[a,b,c] BEATRIZ PEÑA-MOLINO,[b,d] STEPHEN R. RINTOUL,[b,d] AND EDWARD DODDRIDGE[a,b]

[a] *Institute for Marine and Antarctic Studies, University of Tasmania, Hobart, Tasmania, Australia*
[b] *Australian Antarctic Program Partnership, Institute for Marine and Antarctic Studies, University of Tasmania, Hobart, Tasmania, Australia*
[c] *ARC Centre of Excellence for Climate Extremes, University of New South Wales, Sydney, New South Wales, Australia*
[d] *CSIRO Environment, Hobart, Tasmania, Australia*

(Manuscript received 9 March 2023, in final form 28 March 2024, accepted 29 April 2024)

ABSTRACT: The vertically integrated zonal momentum balance of the Antarctic Circumpolar Current (ACC) is dominated by wind stress at the surface and topographic form stress (TFS) at the bottom. It has been argued that wind stress is transferred from the surface to the bottom by transient baroclinic eddies, via interfacial form stress, to establish the balance between wind stress and TFS. However, ocean models indicate TFS responds rapidly to changes in wind stress, suggesting that barotropic processes play a role in this balance. We investigate the dynamics governing the wind–TFS balance of the ACC and its response to wind using an idealized, wind- and buoyancy-driven channel model. We show that the balance is established and maintained at equilibrium by the barotropic dynamics. The balance results from the continuity of the flow, in which the Ekman transport at the surface, balanced by wind stress, is compensated by a return flow at depth, balanced by TFS. This leads to a match between wind stress and TFS which is independent of momentum stresses in the interior. Transient baroclinic eddies oppose the wind-driven isopycnal steepening via eddy buoyancy fluxes, which act to flatten the isopycnals. The eddy-driven isopycnal flattening corresponds to a reduction in the zonal geostrophic shear and thus a redistribution of the zonal momentum in the interior via eddy momentum stresses. The maintenance of the vertically integrated ACC momentum balance by the barotropic dynamics explains the fast response of the wind–TFS balance to changes in wind forcing.

KEYWORDS: Barotropic flows; Continuity equation; Momentum; Ocean dynamics

1. Introduction

The Antarctic Circumpolar Current (ACC) flows around the Antarctic continent without being blocked by lateral boundaries in the latitude band of Drake Passage. The vertically integrated zonal momentum balance of the ACC is dominated by wind stress at the surface and topographic form stress (TFS) at the bottom (e.g., Munk and Palmén 1951). The TFS is generated by the zonal flow interacting primarily with large-scale topographic ridges (e.g., Masich et al. 2015), leading to the formation of ACC meanders and the associated pressure difference across a ridge (e.g., Naveira Garabato et al. 2013; Stewart and Hogg 2017; Bai et al. 2021; Zhang et al. 2023). The momentum balance of the ACC, in particular how the wind stress is communicated from surface to the bottom, has been the focus of research for many decades (e.g., Munk and Palmén 1951; Tréguier and McWilliams 1990; Olbers et al. 2004; Howard et al. 2015). It has been proposed that the momentum imparted by the wind stress at the surface is transferred to the bottom via isopycnal form stresses [vertical Eliassen–Palm (EP) flux] associated with mesoscale eddies (e.g., Johnson and Bryden 1989; Ward and Hogg 2011; Howard et al. 2015). Johnson and Bryden (1989) assumed that the vertical EP flux throughout the water column matches the wind stress at the surface and then used a downgradient eddy heat flux parameterization, relating the EP flux to the vertical shear of the time-mean ACC, to make a prediction of the ACC shear (and transport) in terms of wind stress. Based on their theoretical model, Johnson and Bryden (1989) put forward a mechanistic description of the ACC spinup and equilibration, in which wind stress initially accelerates the ACC zonal flow in the surface layers of the ocean; then, eddies develop from baroclinic instability and transfer the zonal momentum downward, thus deepening the ACC zonal flow until it reaches topography at the bottom, where eddy momentum stresses (EP flux) are balanced by TFS.

In addition to the vertical transfer of the zonal momentum, transient baroclinic eddies have also been shown to flatten the isopycnals via the eddy-induced overturning circulation (e.g., Marshall and Radko 2003; Nikurashin and Vallis 2011). The meridional overturning circulation is described as a residual overturning circulation between the wind-driven and eddy-induced overturning circulations. Wind stress drives the Ekman transport at the surface and corresponding upwelling and downwelling in the interior, forming an overturning circulation, also known as the Deacon cell (Döös and Webb 1994), that steepens isopycnals in the ocean interior. Baroclinic instability resulting from the vertical ACC shear due to steepening isopycnals leads to the generation of mesoscale eddies. On average, the effect of the eddies can be described as an eddy-induced overturning circulation that flattens the isopycnals,

Corresponding author: Xihan Zhang, xihan.zhang@utas.edu.au

DOI: 10.1175/JPO-D-23-0042.1

thus opposing the wind-driven circulation (Andrews and McIntyre 1976). The residual overturning circulation is balanced diabatically by buoyancy fluxes at the surface and diapycnal mixing in the interior (Marshall and Radko 2006; Ito and Marshall 2008; Nikurashin and Ferrari 2013). In the absence of diabatic forcing, the residual overturning circulation vanishes (e.g., Marshall and Radko 2003), leaving the eddy-induced overturning circulation to cancel the wind-driven overturning circulation.

Cancellation between the wind-driven and eddy-induced overturning circulation in the buoyancy budget translates to a match between wind stress at the surface and eddy momentum stresses (EP flux) in the interior—an assumption made by Johnson and Bryden (1989) in their theoretical model. However, the residual overturning circulation does not vanish in the ocean (e.g., Lumpkin and Speer 2007). For example, Masich et al. (2018) diagnosed interfacial form stresses in the Southern Ocean State Estimate (SOSE), showing that they only approximately equaled the wind stress at the surface within the Drake Passage latitude range. Moreover, the authors found that while eddies transferred wind stress vertically, the EP flux was not constant with depth, with its vertical divergence balanced by the Coriolis force associated with the residual overturning circulation (e.g., Rintoul et al. 2001; Ward and Hogg 2011; Marshall et al. 2017).

Ward and Hogg (2011) and Howard et al. (2015) have explored the establishment of the ACC momentum balance from rest. In contrast to the mechanistic description proposed by Johnson and Bryden (1989), Ward and Hogg (2011) report that during the model spinup from rest, in the absence of eddies, TFS at the bottom develops within weeks after wind stress is applied, indicating the importance of fast barotropic dynamics for generating pressure difference across topography. However, when transient eddies are generated from baroclinic instability, in line with the mechanistic description of Johnson and Bryden (1989), Howard et al. (2015) argue that the eddy interfacial form stresses become responsible for the transfer of wind stress from the surface through to TFS at the bottom. In the limit of vanishing residual circulation, a match between wind stress, eddy interfacial form stress, and TFS diagnosed in various isopycnal models has been taken as confirmation that the momentum imparted by the wind is transferred to the bottom by eddies (e.g., Marshall et al. 1993; Ward and Hogg 2011; Howard et al. 2015).

The sequential development of the ACC zonal flow and vertical eddy momentum fluxes transferring momentum to the bottom where it is balanced by TFS, as suggested by Johnson and Bryden (1989), is not consistent with the spinup process for different layers in isopycnal models (e.g., Ward and Hogg 2011). In addition, baroclinic dynamics are expected to adjust on a slow (years) time scale (e.g., Howard et al. 2015). If baroclinic processes alone established the balance between wind stress and TFS, that would imply a relatively slow response of TFS to changes in wind. However, models (Masich et al. 2015; Webb and de Cuevas 2007) show the vertically integrated momentum balance of the ACC responds rapidly to changes in wind forcing. In particular, Webb and de Cuevas (2007) argue for the role of the fast barotropic dynamics in maintaining this balance. In this study, we explore the governing dynamics that establish and maintain the vertically integrated momentum balance of the ACC and describe the role played by the barotropic and baroclinic dynamics using an idealized channel model of the Southern Ocean. Following a similar approach to Ward and Hogg (2011), we identify different stages of the ACC spinup from rest. Specifically, we show that the barotropic dynamics not only establish the vertically integrated momentum balance between wind stress at the surface and TFS at the bottom in the initial spinup stage, as suggested by Howard et al. (2015), but they also maintain the balance in the presence of transient baroclinic eddies at equilibrium. As a consequence, the response of the ACC zonal momentum balance to changes in wind stress from equilibrium is governed by barotropic dynamics and characterized by a fast (weeks) time scale.

The paper is structured as follows. Governing equations, our channel model configuration, and a set of experiments are described in section 2. In section 3, we describe different stages of the flow spinup from rest, during which the vertically integrated momentum balance between wind stress and TFS is established, and evaluate the role played in this balance by the barotropic and baroclinic dynamics. The response of the ACC momentum balance to a doubling of wind stress from equilibrium is discussed in section 4. Finally, a summary, discussion, and implications of the results are presented in section 5.

2. Methods

a. Governing equations

In this study, we analyze the governing dynamics using the depth-coordinate framework, in which the Boussinesq momentum, continuity, and buoyancy equations can be written as follows (e.g., Vallis 2019):

$$\frac{\partial \mathbf{u}}{\partial t} + \mathbf{u}\cdot\nabla\mathbf{u} + f\mathbf{k}\times\mathbf{u} = -\nabla p + b\mathbf{k} + \frac{\partial \boldsymbol{\tau}}{\partial z}, \tag{1}$$

$$\nabla\cdot\mathbf{u} = 0, \tag{2}$$

$$\frac{\partial b}{\partial t} + \mathbf{u}\cdot\nabla b = \frac{\partial B}{\partial z}, \tag{3}$$

where $\mathbf{u} = (u, v, w)$ is the velocity vector, $\mathbf{k}$ is the unit vector in the vertical direction, f is the Coriolis parameter, p is pressure, $\boldsymbol{\tau}$ is viscous stress (both absorbing reference density ρ_0), b is buoyancy, and B is buoyancy flux. Horizontal viscous stresses and buoyancy fluxes are neglected.

Applying Reynolds decomposition,

$$\mathbf{u} = \overline{\mathbf{u}} + \mathbf{u}', \quad p = \overline{p} + p', \quad b = \overline{b} + b', \tag{4}$$

where $\overline{(\cdot)}$ is time and zonal mean and $(\cdot)'$ is a deviation from the mean (i.e., standing and transient eddies), and neglecting nonlinear terms and Reynolds stresses in the momentum equation, we obtain a set of equations governing the mean flow:

$$f\mathbf{k}\times\overline{\mathbf{u}} = -\overline{\nabla p} + \overline{b}\mathbf{k} + \frac{\partial\overline{\boldsymbol{\tau}}}{\partial z}, \tag{5}$$

$$\nabla\cdot\overline{\mathbf{u}} = 0, \tag{6}$$

$$\overline{v}\frac{\partial\overline{b}}{\partial y} + \overline{w}\frac{\partial\overline{b}}{\partial z} = \frac{\partial\overline{B}}{\partial z} - \frac{\partial}{\partial y}(\overline{v'b'}) - \frac{\partial}{\partial z}(\overline{w'b'}). \tag{7}$$

Equation (5) describes the geostrophic and hydrostatic balances in the interior, as well as the Ekman layer dynamics at the surface and bottom. Equation (7) describes the mean buoyancy distribution (i.e., isopycnal slopes) governed by the Eulerian mean circulation and eddy buoyancy fluxes (e.g., Marshall and Radko 2003).

Integrating the zonal component of Eq. (5) in the vertical, we get

$$0 = -\int_{-H}^{\overline{\eta}}\frac{\overline{\partial p}}{\partial x}dz + \overline{\tau_w} - \overline{\tau_b}, \tag{8}$$

where H is depth, η is the surface height, and the terms on the right-hand side from left to right are TFS, wind stress $\overline{\tau_w}$, and bottom frictional drag $\overline{\tau_b}$. Equation (8) is the vertically integrated zonal momentum balance of the ACC, dominated by wind stress and TFS (Masich et al. 2015), the establishment and maintenance of which we explore in this study.

b. *Numerical model configuration*

A zonally re-entrant channel model based on the depth-coordinate Massachusetts Institute of Technology General Circulation Model (MITgcm) (Marshall et al. 1997) is used in this study. The zonal and meridional extent of the model domain is $L_x = L_y = 2000$ km with a depth of 3 km. The model is forced by a prescribed sinusoidal zonal wind stress and heat flux at the surface (Figs. 1a,b). A 1-km-tall, 400-km-wide Gaussian ridge is inserted in the middle of the domain (Fig. 1c). The model horizontal resolution is 10 km in both directions, sufficient to resolve eddies (Fig. 1d). There are 40 vertical levels with the vertical grid spacing varying from 10 m at the surface to around 200 m at bottom. Within a 100-km sponge layer at the northern boundary, temperature is restored to a prescribed exponential profile representing the thermocline in the ocean basin to the north (e.g., Abernathey et al. 2011). Salinity is ignored, and a single-variable linear equation of state is used. All lateral boundaries are set to be free-slip. A linear drag with a coefficient $r = 1.1\times10^{-3}$ m s^{-1} is applied at the bottom. Online diagnostics are saved as daily averages for the first 4 months and annual averages for the entire period of simulations. The model configuration is similar to that in Abernathey et al. (2011) and Abernathey and Cessi (2014) and has recently been used in Zhang et al. (2023), to which the reader is referred for further details. We keep the zonal domain extent the same as in Abernathey and Cessi (2014) but also check that our results hold in a simulation with a tripled zonal extent of the model domain where a stronger deep gyre develops (not shown) (e.g., Jackson et al. 2006; Munday et al. 2015; Nadeau and Ferrari 2015; Patmore et al. 2019). Consistent with the zonal momentum balance for a realistic model in Masich et al. (2015), the full zonal momentum balance in our model is dominated by wind stress and TFS (Fig. 1e).

We carry out several model experiments. To isolate the role of the fast barotropic dynamics (i.e., no baroclinic processes), we carry out a homogeneous experiment by setting the temperature to a constant, 10°C. The surface heat flux and the northern boundary restoring are also disabled in this simulation, while the rest of the model configuration remains the same. This experiment is referred to as homogeneous below, while the reference model configuration described above is referred to as stratified. In our study, we refer to the dynamics (e.g., Ekman layer, surface height gradient, and barotropic zonal flow) that can exist in the absence of stratification as barotropic dynamics. The dynamics that intrinsically depend on stratification (e.g., baroclinic pressure gradient, baroclinic instability, and eddy buoyancy fluxes) are referred to as baroclinic dynamics. Thus, the homogeneous experiment simulates only the barotropic dynamics, while the stratified experiment simulates both the barotropic and baroclinic dynamics. We also carry out experiments with increased wind stress by doubling the amplitude of the wind stress (Fig. 1a) after both the homogeneous and stratified simulations reach equilibrium. These experiments are referred to as double-wind stratified and double-wind homogeneous experiments below. The stratified experiment is run for 100 years from rest to equilibrium. The double-wind stratified experiment is run for 30 years after the amplitude of wind stress is doubled. As the barotropic dynamics adjust on a much faster (months) time scale, the homogeneous and double-wind homogeneous experiments are run for 10 years to equilibrium.

3. Results: Spinup from rest

In this section, we examine the spinup of the flow from rest, in which various components of the full ACC dynamics appear and equilibrate at different stages. We identify three stages of the flow spinup: the Ekman layer dynamics, barotropic (homogeneous) flow dynamics, and baroclinic (stratified) flow dynamics. The first two stages take place within the first 1–2 months, during which the momentum balance between the wind stress at the surface and the TFS at the bottom is established. During this period, the isopycnals do not steepen enough to contribute to the overall dynamics, i.e., there are no significant horizontal density gradients throughout the water column and the flow evolution in the stratified experiment is similar to that in the homogeneous one. The third stage, involving the stratified dynamics, starts as the isopycnals steepen, and the flow begins to depart from the homogeneous case. This stage continues for 50–100 years until the isopycnal steepening is balanced by the eddy-induced isopycnal flattening. We further divide the stratified dynamics stage into two substages: first, corresponding to the initial isopycnal steepening, largely unopposed by the eddies, and second, the final equilibrium stage, in which the eddies develop and oppose the isopycnal steepening. Each stage of the spinup from rest to equilibrium is described in detail below.

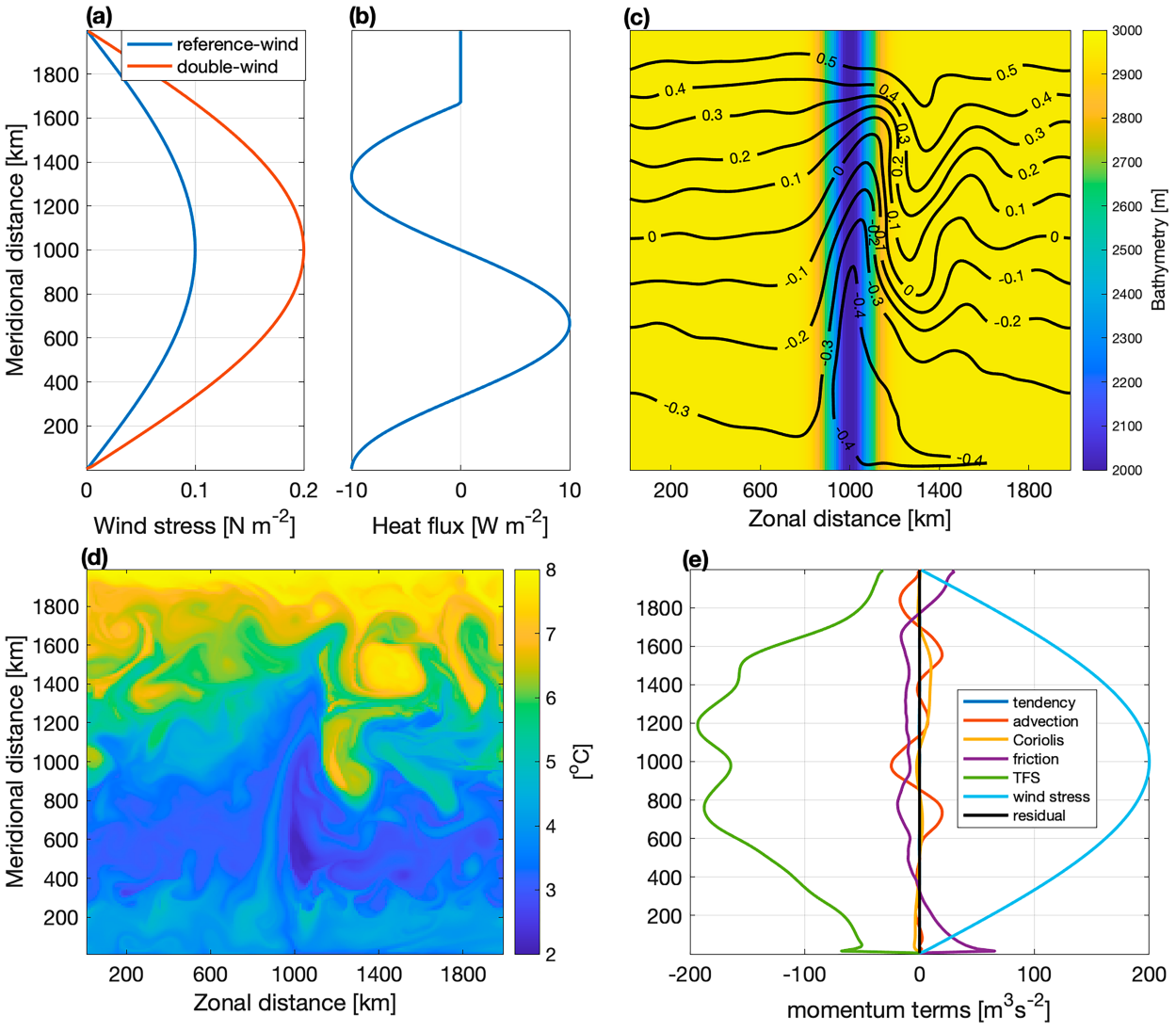

FIG. 1. (a) The zonal wind stress (N m^{-2}), (b) surface heat flux (W m^{-2}), and (c) bathymetry (m) and time-mean sea surface height (m) from the stratified simulation. (d) A snapshot of the sea surface temperature (°C) and (e) time-mean and zonally integrated zonal momentum terms (m^3 s^{-2}) from the stratified simulation.

a. Stage 0: The Ekman layer dynamics

When steady zonal wind stress is applied to a motionless fluid, it first leads to the development of the surface Ekman layer (Fig. 2) (e.g., Pedlosky 1996). The vertically integrated Ekman layer is described by a balance between the zonal wind stress and the Coriolis force corresponding to the meridional Ekman transport V_E:

$$-fV_E = \overline{\tau_w}. \tag{9}$$

Within the Ekman layer, there is a balance between frictional stresses and the Coriolis force at each depth level. Frictional stresses vanish below the Ekman layer. Thus, while the wind stress is in fact transferred downward by frictional stresses, the transfer is limited to the Ekman layer depth. To illustrate the development of the Ekman layer in the models, a time series of the zonally integrated (and meridionally averaged) meridional transport within the Ekman layer, chosen as the upper 100 m based on the vertical profile of velocity (not shown), in both stratified and homogeneous simulations is shown in Fig. 3a. Both models converge to a theoretical Ekman transport value (for our model parameters) of 1.42 Sv (1 Sv $\equiv 10^6$ m^3 s^{-1}) after a few days and then oscillate around this value. The oscillations are due to transient adjustments of the flow to the sudden impact of wind stress at the beginning of the simulation and decay away after about 30 days. The decay time scale is controlled by bottom friction, as we discuss below. The Ekman transport in the homogeneous and stratified simulations is similar, and both remain steady for the rest of the simulation. In summary, wind stress at the surface is balanced by the Coriolis force within the Ekman layer, and the balance is achieved in the first few days. This balance,

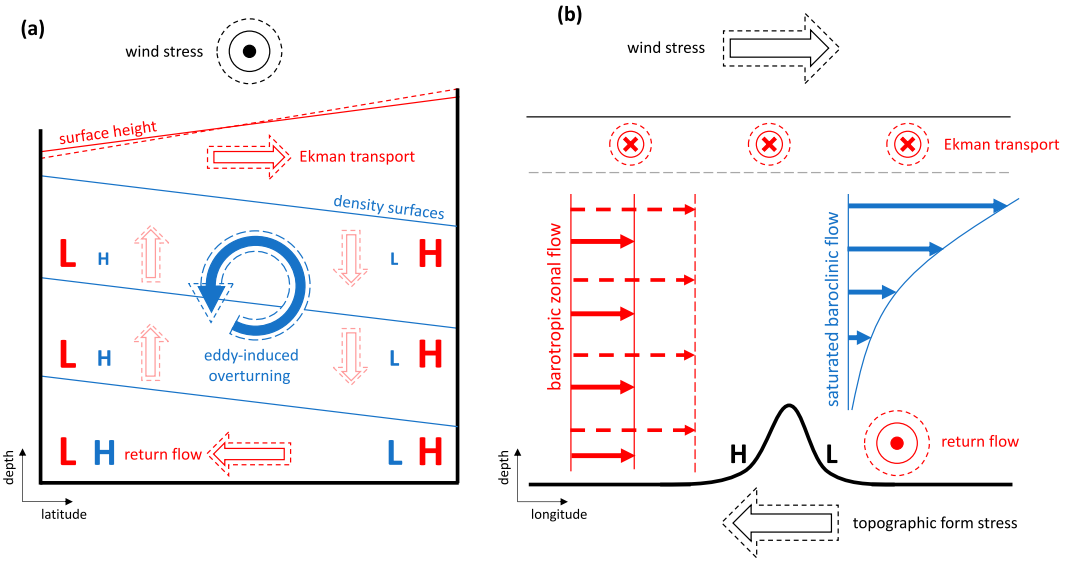

FIG. 2. A schematic illustrating the establishment of the vertically integrated zonal momentum balance of the ACC and its adjustment to an increase in zonal wind stress in (a) meridional and (b) zonal view. Red and blue colors indicate barotropic and baroclinic dynamics, respectively. The "H" and "L" stand for high and low pressure anomaly, respectively. Solid lines represent the equilibrated reference case, and dashed lines indicate a response to the increased wind stress. The wind–TFS balance is established as follows. The westerly wind stress drives the Ekman transport which builds up the sea surface height slope and thereby the barotropic pressure gradient (and zonal flow) at depth. The barotropic zonal flow interacts with the ridge to create the TFS through a zonal pressure gradient across the ridge. Through geostrophy, this zonal pressure gradient drives the meridional return flow at the bottom compensating for the Ekman transport at the surface (hence TFS balancing wind stress). Isopycnals are steepened by the wind-driven upwelling creating a baroclinic pressure gradient which opposes the barotropic pressure gradient and hence acts to reduce TFS and the return flow. As a result, the sea surface height slope continues to increase to compensate for the effect of baroclinicity and maintain TFS and the return flow until baroclinic eddies develop and oppose the wind-driven steepening through the eddy-induced isopycnal flattening. The balance between wind stress and TFS is achieved when the volume budget (Ekman transport balanced by return flow) is closed. The isopycnal slopes are insensitive to changes in wind, and hence, the fast barotropic dynamics are responsible for the adjustment of the system to the increased wind stress.

however, leads to the meridional Ekman transport which produces an imbalance in the volume budget (continuity). Thus, from this stage onward, the evolution of the flow is governed by the volume budget adjustments.

b. *Stage 1: Barotropic (homogeneous) dynamics*

The northward Ekman transport moves water from south to north, leading to a buildup of the meridional surface height gradient. Changes in the zonally averaged surface height are governed by the vertically integrated and zonally averaged continuity equation:

$$\frac{\partial \overline{\eta}^{x}}{\partial t} + \frac{\partial}{\partial y}\int_{-H}^{\eta} \overline{v}^{x} dz = 0. \tag{10}$$

The second term in Eq. (10) includes a net meridional volume transport which, in the absence of the return flow, consists only of the northward Ekman transport. The buildup of the surface height gradient continues until a southward return flow at depth develops and compensates the surface Ekman transport, i.e., the net meridional volume transport vanishes. The temporal evolution of the surface height in both models is shown in Figs. 4a and 4b, and the corresponding surface height differences between two latitudes, one in the north and one in the south, are shown as a function of time in Fig. 4e. We can see that, in the homogeneous simulation, water quickly piles up in the northern part of the domain and reaches a steady meridional gradient (with a north–south surface height difference of about 5 cm) after 1 month following initial transient adjustments. In the stratified simulation, the surface height evolution is similar to that in the homogeneous simulation in the first month or so, suggesting that the dynamics are dominated by its barotropic component. In the following months, the sea surface height in the stratified model continues to increase monotonically, which we explain in detail next in stage 2.

The buildup of the meridional surface height gradient is accompanied by a barotropic pressure gradient at all depths and thus drives a zonal barotropic flow $\overline{u}_{\mathrm{bt}}$ in the interior governed by the zonally averaged meridional geostrophic balance:

$$f\overline{u}_{\mathrm{bt}} = -g\frac{\partial \overline{\eta}}{\partial y}, \tag{11}$$

where g is gravity. The dominance of the barotropic flow in this first stage is evident in both the homogeneous and stratified

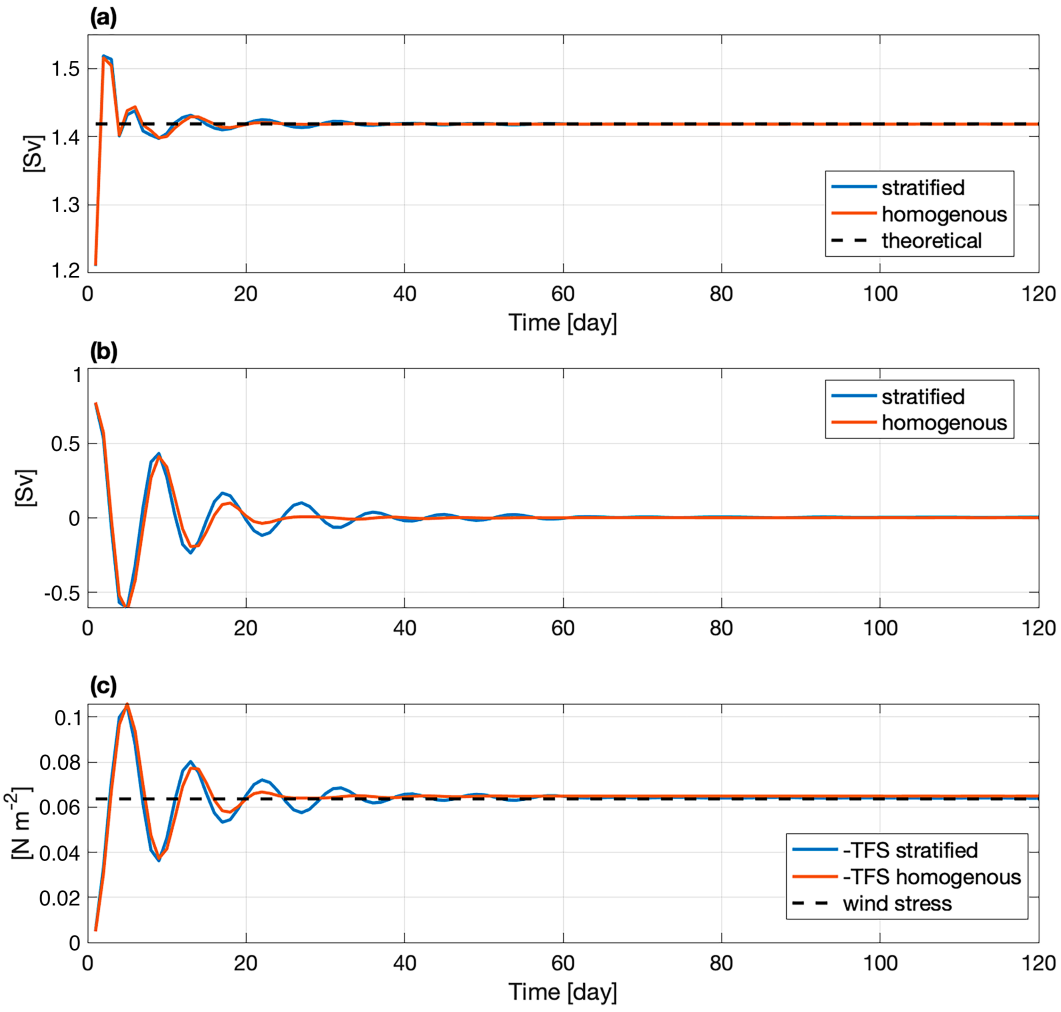

FIG. 3. Time series of (a) the zonally integrated and meridionally averaged Ekman transport (Sv) from stratified and homogeneous simulations. The theoretical prediction for the Ekman transport is shown by the dashed line. Time series of (b) meridionally averaged total meridional transport (Sv) and (c) meridionally averaged TFS (N m^{-2}).

simulations shown with the vertical structure of zonal velocity in Figs. 4c and 4d, where the signal in the top 100 m or so corresponds to the Ekman layer in the model. The evolution of the zonal barotropic flow is consistent with changes in the surface height gradient and, in the first month, is similar between the homogeneous and stratified simulations.

As soon as the zonal barotropic flow appears, it interacts with the bottom. In a flat bottom case (not shown), it is opposed by the bottom frictional drag and thus leads to the formation of the bottom Ekman layer, in which the southward bottom Ekman transport brings water from north to south (i.e., frictional return flow). In a ridge case considered here, the zonal barotropic flow interacts with the ridge, leading to the formation of a meander (e.g., Zhang et al. 2023). The pressure difference across the ridge associated with the zonal flow and its meander results in TFS, the magnitude of which scales with the zonal barotropic flow (Bai et al. 2021). In response to TFS or the pressure difference in the valley below the height of the ridge, a meridional geostrophic flow develops, which returns water from north to south (i.e., geostrophic return flow), with the total volume transport V_R given by

$$fV_R = \int_{-H}^{-D} \frac{\overline{\partial p}}{\partial x} dz, \tag{12}$$

where D is the depth of topography and the right-hand side is TFS.

In both simulations, the return flow (not shown) increases rapidly reaching the value of the surface Ekman transport in the first month or so and then remains constant throughout the simulation. Consistently, the total meridional transport (Fig. 3b), the sum of the Ekman and return flow transports is positive at the beginning of the simulation (thus corresponding to the surface pileup in the north) in both simulations but decreases to zero in about a month in the homogeneous simulation, and to a small, 0.002 Sv (0.1% of the Ekman transport), residual in the stratified simulation. The small residual in the stratified simulations corresponds to a continuing gradual increase in the surface

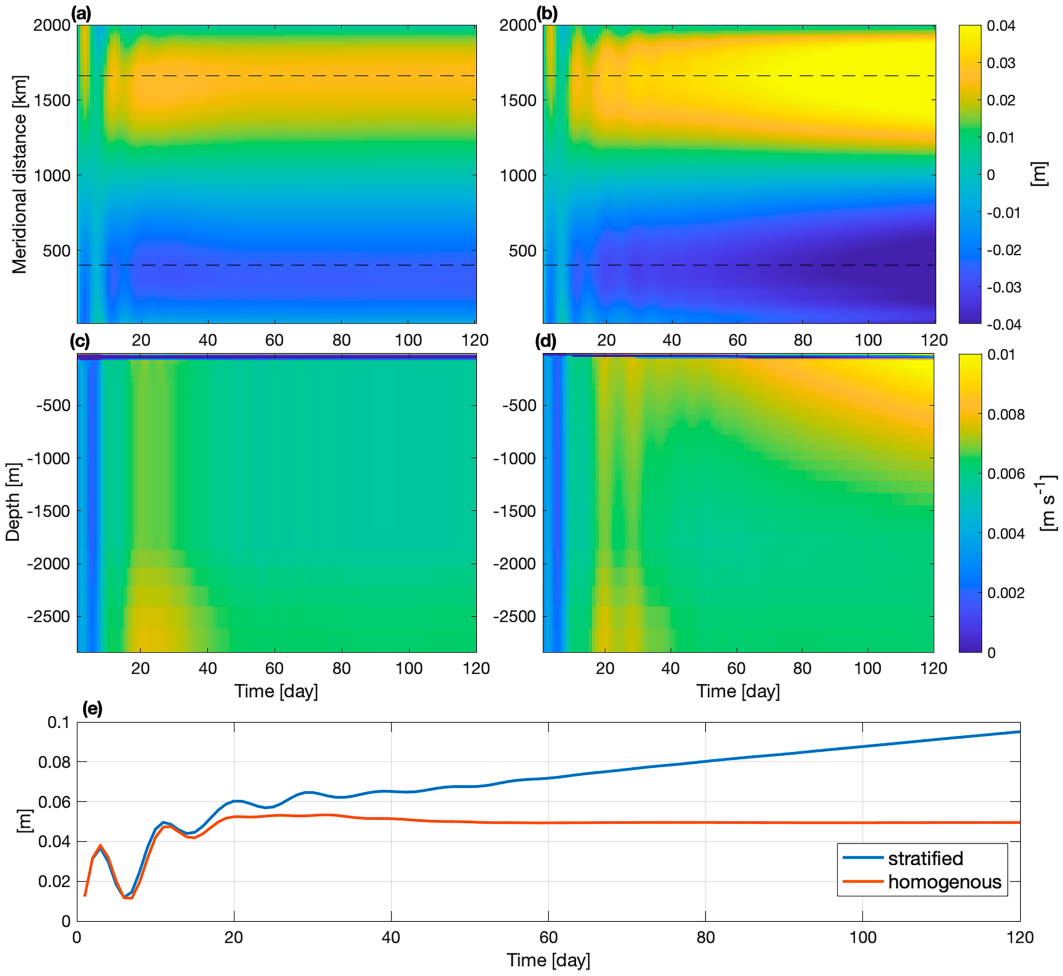

FIG. 4. Evolution of the zonally averaged sea surface height (m) from (a) homogeneous and (b) stratified simulation. Evolution of the zonally averaged zonal velocity (m s^{-1}) profile at $y = (1/2)L_y$ in (c) homogeneous simulation and (d) stratified simulation. (e) Time series of the sea surface height difference (m) between $y = 1600$ km and $y = 400$ km, marked by dashed lines in (a) and (b).

height gradient beyond the stage 1 time period, a response discussed in stage 2 below.

Our results show that the surface and bottom stresses are related via the total volume budget, requiring that the net meridional volume transport vanishes at equilibrium. At equilibrium, the return flow transport at depth exactly compensates for the Ekman transport at the surface, and hence, the wind stress matches the TFS, which initially arises from zonal flow interacting with the ridge and equilibrates through the return flow. Consistent with this, the time series of TFS in Fig. 3c shows that the vertically integrated momentum balance between the wind stress and TFS is achieved within the first month, during which the evolution of the stratified simulation is similar to that of the homogeneous simulation. To further demonstrate that TFS results from the flow continuity (return flow) rather than simply in response to wind stress at the surface, we present an additional idealized experiment in the appendix (Experiment 1), in which we force the flow with uniform wind stress at the surface in a doubly periodic model domain. The results show that the flow equilibrates with zero TFS across the ridge. In this case, the vertically integrated zonal momentum balance is between wind stress and Coriolis force associated with the northward Ekman transport. Given that there is no return flow at depth in this experiment (uniform wind stress in a doubly periodic domain drives a uniform northward Ekman transport), no TFS develops at the bottom.

The vertically integrated momentum balance between the wind stress at the surface and the TFS at the bottom and the connection to the volume budget have been previously discussed for an equilibrated ACC flow (Olbers 1998). In this study, we reconcile this idea with the buildup of the TFS and extend the discussion to the establishment of this balance from rest in response to the westerly wind. In summary, the establishment goes as follows (red solid lines in Fig. 2). The westerly wind drives the Ekman layer with the corresponding northward Ekman transport, which is achieved in the first few days and remains steady for the rest of the simulation. The northward Ekman transport is initially unbalanced in the

volume budget sense and leads to an increase in surface height in the north. The resulting meridional surface height gradient creates a barotropic pressure gradient throughout the water column and thus drives a zonal barotropic flow, which increases with the surface height gradient. The zonal barotropic flow at the bottom interacts with the ridge to produce the TFS, i.e., a zonal pressure gradient across the ridge/valley, the magnitude of which increases with the magnitude of the zonal barotropic flow (and hence with the surface height gradient). The zonal pressure gradient in the valley corresponds to a return flow that opposes the Ekman transport at the surface. Thus, the surface height in the north continues piling up until the return flow at depth spins up and matches the Ekman transport at the surface. When the southward return flow compensates for the northward Ekman transport, TFS at the bottom equilibrates and matches wind stress at the surface. A characteristic time scale of the barotropic (homogeneous) dynamics in stage 1 is controlled by bottom friction (Bai et al. 2021) and also damps initial transient oscillations. A spindown time scale of the barotropic flow by bottom friction is given by Hr^{-1}, where H is the ocean depth and r is a linear bottom friction coefficient. Substituting the model parameters from section 2, the time scale is approximately 30 days, which is consistent with the adjustment time scale of 1 month seen in stage 1.

c. *Stage 2: Baroclinic (stratified) dynamics*

The surface Ekman transport and associated return flow at depth generated in stage 1 are connected through downwelling in the north and upwelling in the south, thus forming the wind-driven overturning cell (red arrows in Fig. 2a), also known as the Deacon cell (Döös and Webb 1994). The wind-driven overturning circulation steepens the isopycnals by rearranging buoyancy in the system—it transports buoyancy (or heat) away from Antarctica—thereby modifying the meridional pressure gradient, and hence the zonal baroclinic flow, in the interior (blue solid lines in Fig. 2). As we show below, the modification of the pressure gradients by the baroclinic dynamics is compensated by the barotropic dynamics in order to maintain the TFS at the bottom. The transient adjustment continues until the wind-driven overturning circulation is balanced by the eddy-induced overturning circulation, and the buoyancy and volume budgets are closed.

1) STAGE 2A: ISOPYCNAL STEEPENING

The isopycnal steepening is a much slower process than the barotropic adjustments in stage 1 because vertical velocity magnitudes are small. For instance, for a typical vertical velocity of 10^{-6} m s^{-1}, characteristic of the Ekman-driven upwelling, it takes about 3 years to lift the isopycnals by 100 m. Although isopycnals begin to steepen as soon as the surface Ekman transport and return flow appear, the corresponding horizontal density gradients are weak and do not contribute significantly for the first 1–2 months. While small, this isopycnal steepening explains minor differences between the stratified and homogeneous simulations seen during the first 1–2 months in stage 1, with the overall dynamics still dominated by the barotropic dynamics. This can be further seen in the time evolution of the barotropic and baroclinic zonal transports (Fig. 5a) where the barotropic transport is computed from the bottom velocity. The total zonal transport is dominated by its barotropic component in the first 1–2 months, while the baroclinic transport (due to density gradients) catches up and dominates afterward.

The isopycnal steepening in stage 2a (Fig. 6) generates a baroclinic pressure gradient due to density variations at depth, which opposes the barotropic pressure gradient established in stage 1. This is a result of dense fluid accumulating below the low surface height in the south and light fluid accumulating below the high surface height in the north. Thus, the isopycnal steepening acts to reduce the meridional pressure gradient near the bottom established by the barotropic dynamics in stage 1, and therefore, it acts to reduce the return flow. A slight reduction of the return flow by the baroclinicity (Fig. 3a) creates an imbalance in the total meridional volume transport, leading to a continuing buildup of the surface height gradient in stage 2a seen in Fig. 4b. This increase in the surface height gradient is governed by the same rapid barotropic dynamics from stage 1. The surface steepening continues throughout stage 2 to maintain the return flow (and hence TFS) at depth against the tendency for slow isopycnal steepening to reduce the deep pressure gradients that drive the return flow and TFS—i.e., the barotropic flow adjusts to compensate for the effect of baroclinicity. Despite major changes in the baroclinic part of the flow (e.g., isopycnal steepening and transient eddy generation), TFS remains steady for the entire period of the simulation following stage 1 (Fig. 3c).

The baroclinic pressure gradient varies with depth and leads to a vertically varying zonal geostrophic flow $\overline{u}_{\mathrm{bc}}$ governed by the zonally averaged meridional momentum (thermal wind) balance:

$$f\frac{\partial \overline{u}_{\mathrm{bc}}}{\partial z} = -\frac{\partial \overline{b}}{\partial y}. \tag{13}$$

The sheared zonal flow keeps accelerating as isopycnals are steepening (Fig. 4d), also shown by a continuing baroclinic transport increase in Fig. 5. Steady (linear) acceleration of the baroclinic flow lasts for about 6 years, corresponding to isopycnal uplift of a few hundred meters (Fig. 6), after which transient eddies are generated and the acceleration slows down, as discussed in the next section. At this stage, baroclinic transient eddies only start to develop and are characterized by weak vertical EP fluxes in the interior (Fig. 7d). We compute the vertical component of the cross-stream EP flux $\mathcal{E}^z$ following Thompson and Naveira Garabato (2014) as

$$\mathcal{E}^z = \frac{f}{\overline{\theta}_z}\overline{\mathbf{u}'_H\theta'}\cdot\mathbf{n}_\perp, \tag{14}$$

where θ is temperature, $\mathbf{u}_H = (u, v)$ is the horizontal velocity vector, $\mathbf{n}_\perp$ is the unit vector perpendicular to mean SSH contours, overbar represents time averages, and primed quantities are deviations from the time averages. Acceleration and deceleration of the along-stream mean flow by eddies occur at

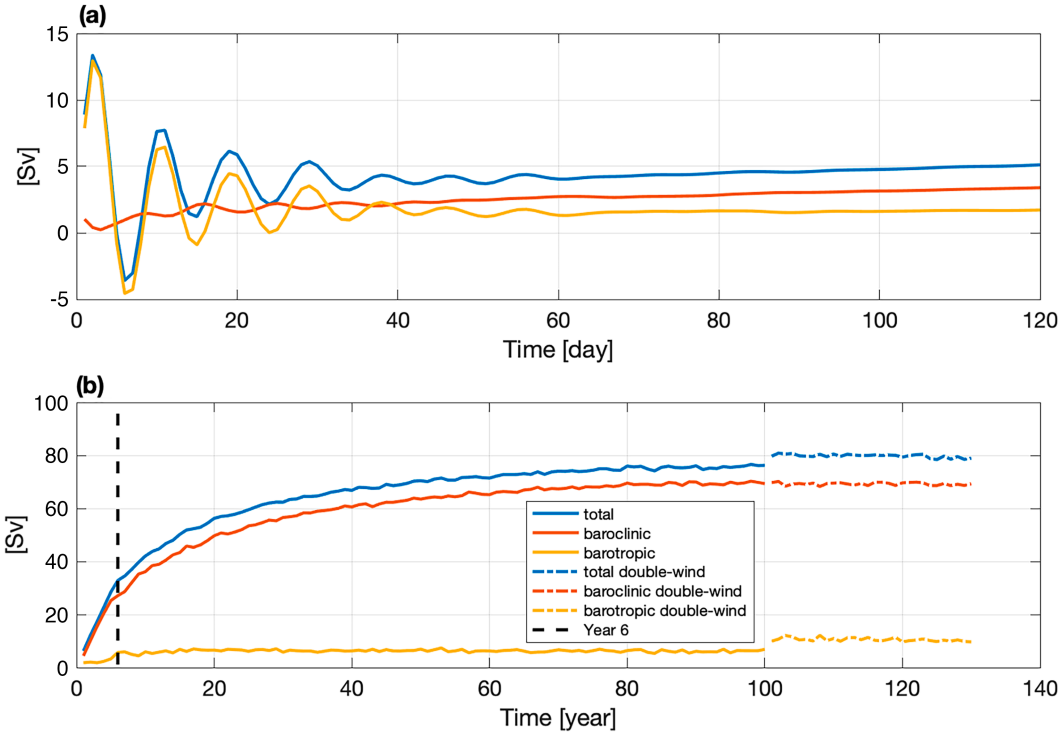

FIG. 5. Time series of the total, barotropic, and baroclinic zonal transports (Sv) upstream of the ridge for (a) the first 4 months and (b) the entire 100-yr period of the stratified (solid) and double-wind stratified (dashed) simulations. Year 6 is marked as a black dashed line.

depths of convergence and divergence of the EP flux, respectively (Thompson and Naveira Garabato 2014).

2) STAGE 2B: EQUILIBRATION BY EDDIES

When the isopycnals are steep enough for baroclinic instability to occur, after roughly 6 years in our model, transient eddies are generated from the instability of the vertically sheared zonal geostrophic flow (e.g., Vallis 2019). Transient eddies transfer buoyancy southward. As a result, transient eddies tend to flatten the isopycnals and hence oppose the wind-driven isopycnal steepening, which dominates in stage 2a. The mean ACC isopycnals are governed by Eq. (7), which can be written in the following form (Marshall and Radko 2003):

$$J(\overline{\Psi} + \Psi^*, \overline{b}) = \frac{\partial B}{\partial z}, \tag{15}$$

where J is a Jacobian operator, representing advection in the meridional and vertical plane; $\overline{\Psi}$ is the mean streamfunction, representing the wind-driven overturning circulation; and Ψ^* is the eddy-induced overturning streamfunction given by

$$\Psi^* = \frac{\overline{v'b'}}{N^2}, \tag{16}$$

where N is stratification. Thus, the buoyancy distribution is governed by the wind-driven overturning circulation steepening isopycnals, eddy-induced overturning circulation flattening isopycnals, and diabatic transformations balancing the total (residual) overturning circulation (e.g., Abernathey et al. 2011; Youngs and Flierl 2023) in the interior and/or at the surface.

In the limit of a weak residual circulation (i.e., weak diabatic transformations), the isopycnals equilibrate when

$$J(\overline{\Psi} + \Psi^*, \overline{b}) \approx 0, \tag{17}$$

implying that the eddy-induced overturning circulation cancels the wind-driven overturning circulation. In other words,

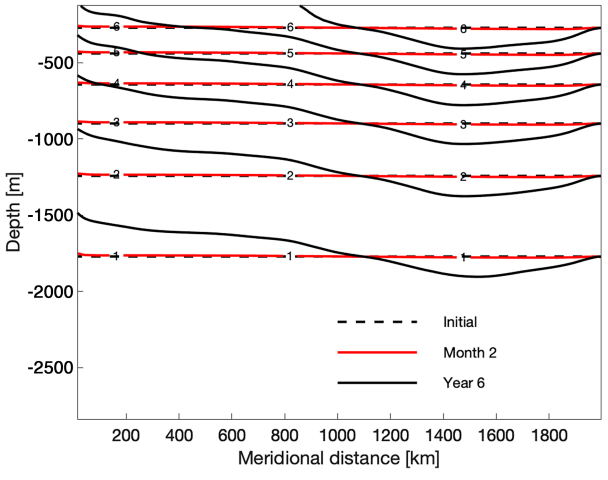

FIG. 6. Zonally averaged isotherms (°C) from the stratified simulation illustrating stage 0, stage 1, and stage 2a isopycnal slopes.

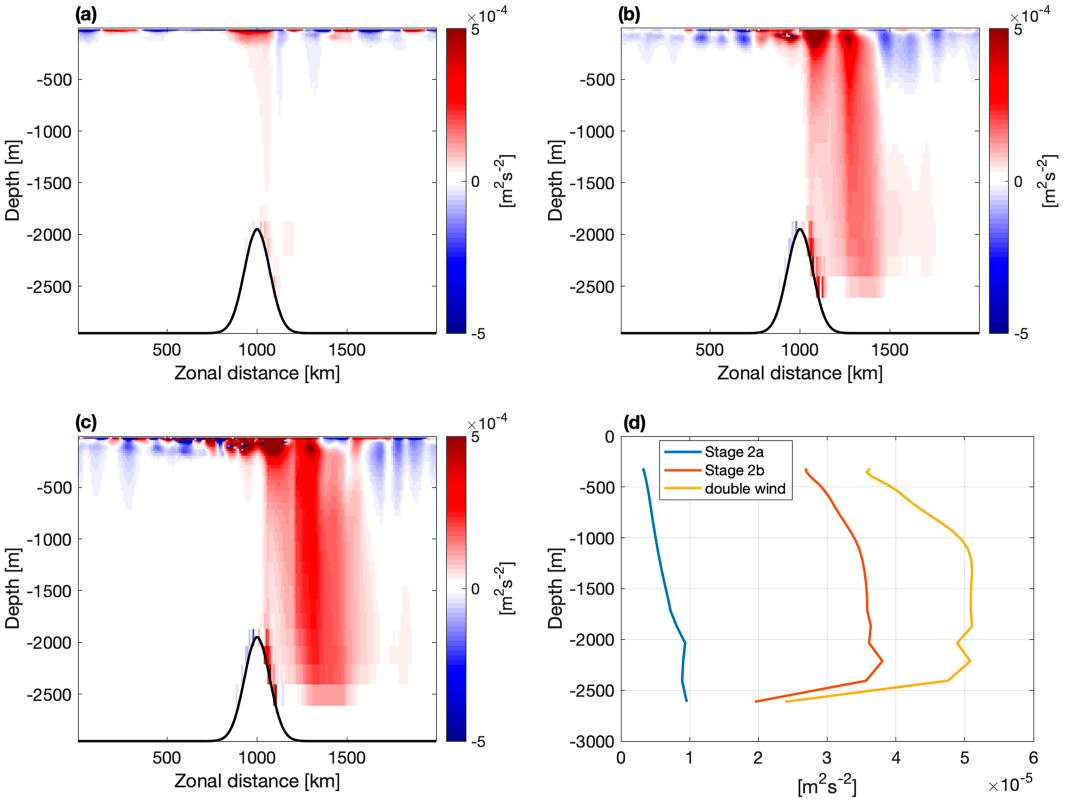

FIG. 7. Time-averaged and cross-stream-averaged vertical component of EP flux ($m^2\ s^{-2}$) for (a) stage 2a, (b) stage 2b, (c) double-wind experiment, and (d) zonally averaged EP flux in (a)–(c). EP flux values in the upper 300 m affected by weak stratification within the mixed layer are not plotted.

eddies (via eddy buoyancy fluxes) transport buoyancy to the south at the same rate as the wind (via Ekman transport and wind-driven upwelling) transports it to the north. In our stratified simulation, the onset of baroclinic instability is reflected by a reduction of baroclinic transport acceleration at around year 6 in Fig. 5b. Around this time, transient eddies appear and start to oppose the isopycnal steepening, thus hindering a further increase of the baroclinic pressure gradient. The time series of vertically and zonally integrated heat transport components evaluated at midlatitude (Fig. 8) demonstrates the equilibration of the heat (buoyancy) budget of the region south of this latitude; when the total heat transport equals the integrated surface heat flux, the heat budget is equilibrated. While, in the first 10–20 years, the eddy heat transport is weak and the total ocean heat transport is dominated by the northward Ekman component, the eddy heat transport develops and eventually opposes the Ekman heat transport. The heat transport in the Ekman layer reduces with time as a result of surface temperature changes as the model equilibrates. The total ocean heat transport, the sum of the mean and eddy heat transport components, approaches the value of the integrated surface heat flux, hence closing the total heat (buoyancy) budget at around year 80 of the simulation. The equatorward total heat transport at the beginning of the simulation results from the unbalanced equatorward heat (buoyancy) transport by the wind-driven circulation (i.e., isopycnal steepening in stage 2a), which is then compensated by the poleward heat (buoyancy) flux due to transient eddies at the end of the simulation, marking a closure of the buoyancy budget and complete equilibration of the flow.

During the adjustment of the buoyancy budget by the wind-driven and eddy-induced overturning circulation, isopycnal slopes are changing, redistributing buoyancy in the meridional direction and hence zonal geostrophic (thermal wind) shear in the vertical. In particular, the role of transient eddies in this adjustment is to flatten the isopycnals via poleward eddy buoyancy fluxes, corresponding to a reduction of the geostrophic (thermal wind) shear by the downward eddy momentum (EP flux) transfer. This is equivalent to the upward (downward) transfer of westward (eastward) momentum in density coordinates described in Ward and Hogg (2011). The EP flux concentrates within the meander region downstream of the ridge, where it transfers eastward zonal momentum downward (Fig. 7). A horizontally averaged profile of EP flux corresponds to mean flow deceleration (EP flux divergence) at the surface and acceleration (EP flux convergence) at depth, thus redistributing the zonal geostrophic momentum in the vertical. Throughout this adjustment of the stratified dynamics (stage 2), the wind–TFS balance remains unchanged. To maintain the return flow, and thereby TFS, in the presence of the opposing baroclinic pressure gradient at depth, the meridional surface height gradient keeps increasing throughout

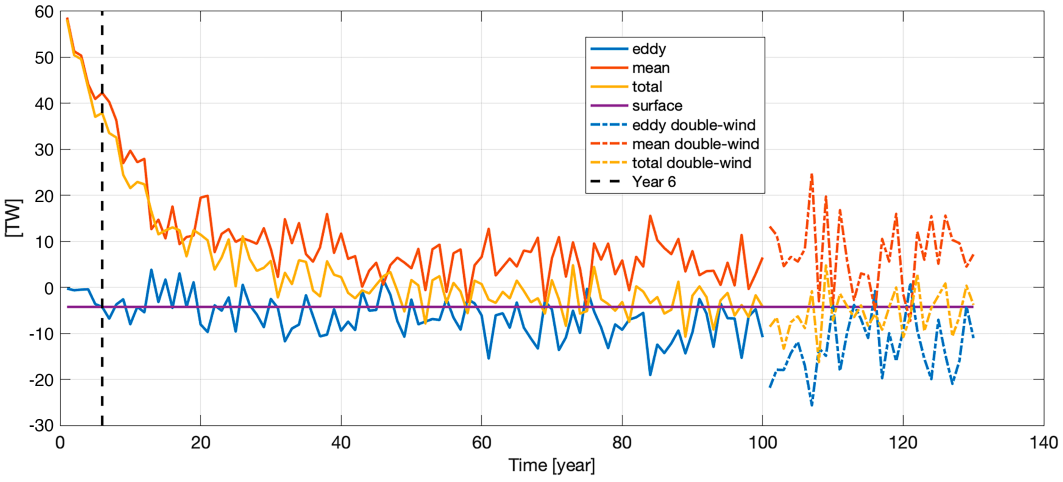

FIG. 8. Time series of heat budget components (TW) for a region south of midlatitude ($y = 1000$ km) for the stratified (solid) and double-wind stratified (dashed) simulations. The surface component of the heat budget is computed as an area integral of the surface heat flux south of the midlatitude and plotted with a minus to match the total ocean heat flux.

the entire simulation, reaching a north–south surface height difference of up to 1 m (Fig. 9). To further support the argument that the eddy momentum stresses (EP flux) redistribute geostrophic shear in the interior rather than transfer wind stress from the surface to the TFS at the bottom, we present an additional idealized simulation (Experiment 2) in the appendix. In this simulation, we add interior temperature restoring to the simulation with the doubly periodic domain forced by uniform wind stress at the surface (Experiment 1 in the appendix) to steepen the isopycnals and generate baroclinic eddies. As in Experiment 1, there is no return flow, and despite the existence of a vigorous baroclinic eddy field that transfers momentum downward in the interior through EP fluxes, TFS across the ridge does not develop.

The time scale characterizing the adjustment of the baroclinic (stratified) dynamics (stage 2) is controlled by transient eddies. Allison et al. (2011) discussed a time scale of the thermocline depth adjustment by eddies given by $L_y^2 K_{\mathrm{GM}}^{-1}$, where L_y is the meridional extent of the domain and K_{GM} is Gent–McWilliams eddy diffusivity (Gent and Mcwilliams 1990).

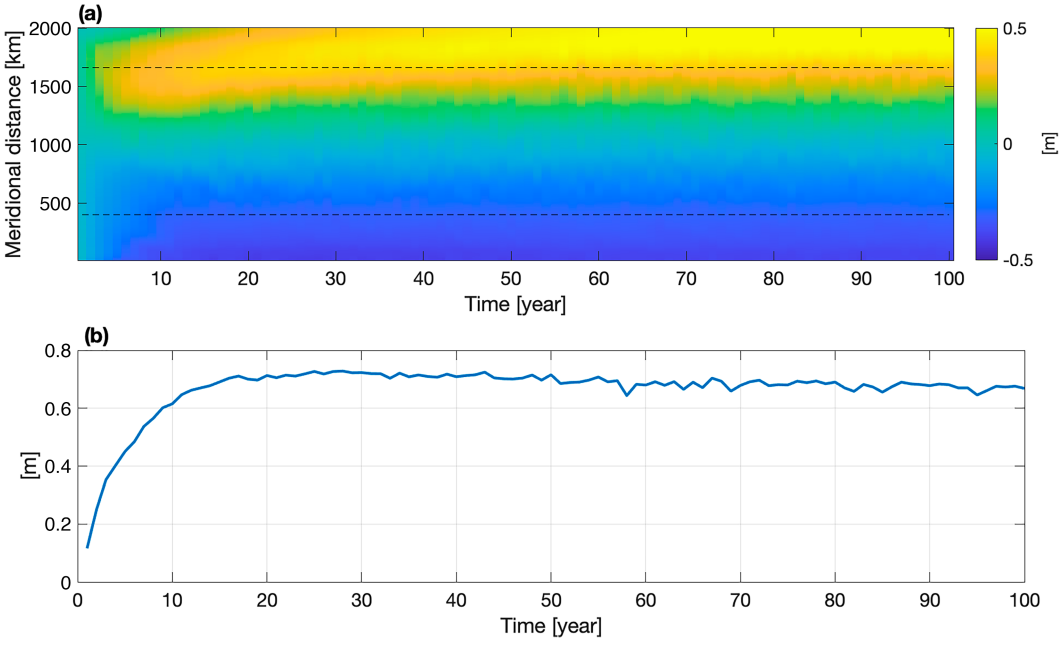

FIG. 9. (a) Evolution of the zonally averaged sea surface height (m) in the stratified simulation. (b) Time series of the sea surface height difference (m) between $y = 1600$ km and $y = 400$ km, marked by dashed lines in (a).

This scaling represents a baroclinic flow spindown by eddies (analogous to the barotropic flow spindown by bottom friction in stage 1), i.e., it is the time that it would take the eddies to flux buoyancy across the domain meridionally (hence flatten the isopycnals) in the absence of wind. Taking a typical value $K_{GM} = 500\ m^2\ s^{-1}$ (e.g., Marshall and Radko 2003), the time scale for the stage 2 equilibration is around 60 years, consistent with the flow equilibration time scale seen in the stratified simulation.

4. Results: Doubling of the wind

In this section, we explore the response of the full dynamics to changes in wind. We double the amplitude of the wind stress in our stratified simulation after 100 years when the simulation is equilibrated. We show below that the barotropic dynamics are again responsible for the adjustment of the momentum balance in response to changes in the wind. We first illustrate that the baroclinic dynamics, i.e., isopycnal slopes and thus the baroclinic ACC transport, are saturated, and hence, there is no readjustment of the baroclinic pressure gradient at depth in response to wind that would need to be rebalanced by the barotropic dynamics (stage 2 above). Therefore, it is only the stage 1 processes that need to operate to adjust the return flow to balance the doubled Ekman transport and hence establish TFS to match the doubled wind stress (dashed lines in Fig. 2).

Consistent with previous studies (e.g., Straub 1993; Munday et al. 2013), the baroclinic transport component is insensitive to the increased wind in the stratified simulation (Fig. 5b). Averaging transports in both stratified and double-wind stratified experiments over the last 20 years shows that the increase in total transport is due to an increase in the barotropic transport (4 Sv, or about 100%, increase), while the baroclinic transport shows only a 0.2% change (around 0.1 Sv). Correspondingly, the isopycnal slopes in the double-wind stratified experiment do not show a noticeable change in response to the wind change (Fig. 10), implying that there is little rearrangement of buoyancy in the ocean interior in response to the wind change.

On the other hand, the results show that there is a fast response to the wind in the surface height gradient and TFS at the bottom, maintained by the barotropic dynamics (stage 1). In response to the doubling of wind stress, the northward Ekman transport doubles, therefore piling up more water in the north, until it is compensated by the return flow. The evolution of the zonally averaged sea surface height (Fig. 11a) shows a fairly steady surface height. However, from stage 2 above, it should be noted that at equilibrium, most of the sea surface height gradient (over 90%) compensates for the baroclinicity: only about 5 cm of the sea surface height difference created during stage 1 is needed to drive the return flow. In agreement, the difference between the northern and southern latitudes in Fig. 11b shows some transient adjustments in the first month, as in stage 1 above, followed by a few centimeter increase in the surface height difference, a change needed to adjust the return flow to changes in the wind. The evolution of the surface height slope in response to the doubling of the wind is similar in terms of amplitude, phase, and frequency to that in Fig. 4b implying that the response is dominated by the barotropic dynamics.

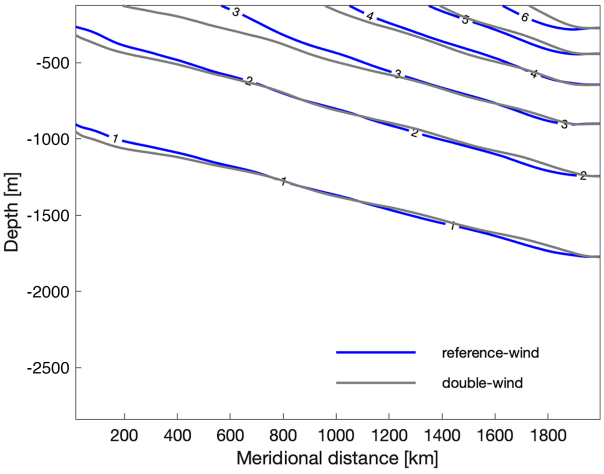

FIG. 10. Zonally averaged and time-averaged isotherms (°C) illustrating isopycnal slopes at equilibrium for both the reference and doubling wind experiments.

To confirm that the readjustment of the stratified flow to a doubling of the wind is governed by the barotropic dynamics, we compare the response of the stratified and homogeneous simulations to wind, as before. We compare the evolution of the total meridional transport and TFS between the double-wind stratified and double-wind homogeneous experiments (Fig. 12). The results show that both simulations are characterized by an initial imbalance in the total meridional transport, corresponding to a surface height buildup of a few centimeters. As opposed to the adjustments during the spinup of the flow, the total meridional transport in the double-wind stratified simulation nearly vanishes after 1 month (residual of 8×10^{-4} Sv) because the isopycnals are insensitive to wind, and hence, the mean and eddy heat fluxes remain balanced (Fig. 8b). Consistent with the eddy heat fluxes, the eddy momentum stresses (EP flux), redistributing the zonal geostrophic shear in the vertical, double in response to the doubling of the winds (Fig. 7). TFS evolves on a similar time scale to the return flow and also adjusts in a month (Fig. 12). Overall, the adjustment and re-equilibration are similar in the double-wind stratified and double-wind homogeneous simulations, confirming that the stratified ACC flow with eddies readjusts to changes in wind via the barotropic dynamics. In summary, our results show that the barotropic dynamics not only establish the vertically integrated zonal momentum balance between wind stress and TFS but also maintain it in response to changes in wind.

5. Summary and discussion

The vertically integrated zonal momentum balance of the ACC is dominated by wind stress at the surface and TFS at the bottom. We investigate the dynamics governing the wind stress–TFS balance of the ACC and evaluate the role of

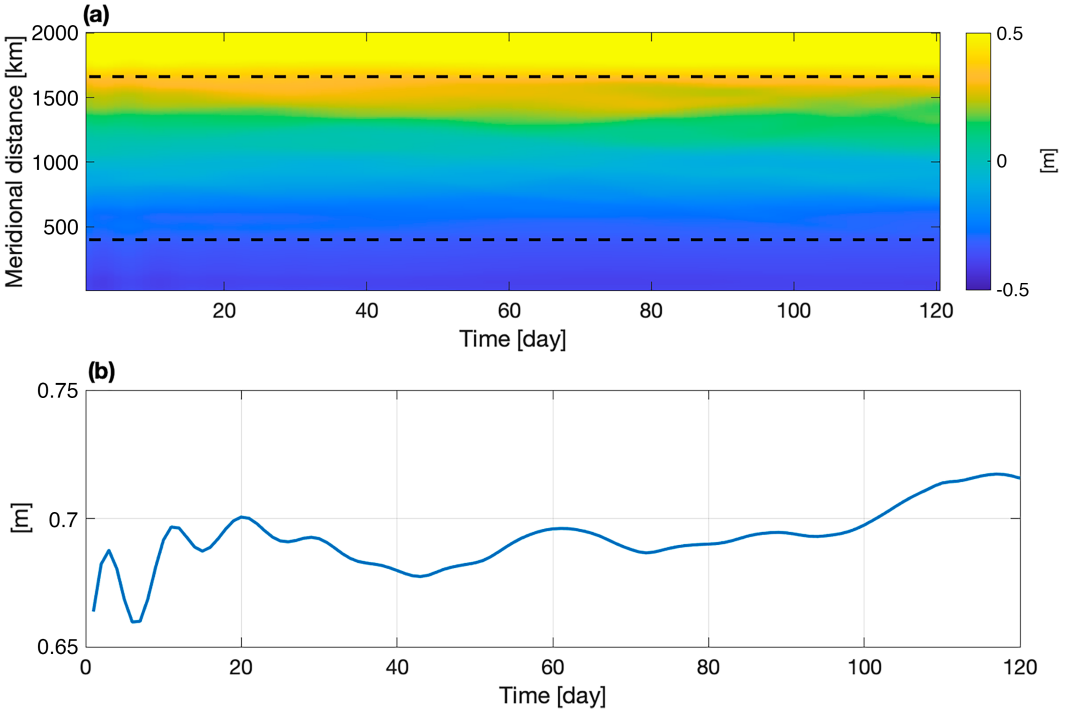

FIG. 11. (a) Evolution of the zonally averaged sea surface height (m) for the first 4 months after doubling the wind. (b) Sea surface height difference (m) between the latitudes marked with dashed lines in (a) in the stratified simulation.

barotropic (homogeneous) and baroclinic (stratified) dynamics during the spinup of the ACC and its response to wind. We find that the balance is maintained by the barotropic dynamics—i.e., Ekman layer, surface height gradient, and zonal barotropic flow—and holds with or without eddies.

The establishment of the wind–TFS balance is achieved in stages as follows. In stage 0 (within the first few days), the westerly wind sets the northward surface Ekman transport. In stage 1 (during the first month), the Ekman transport piles up water in the north, thus generating a meridional sea surface height gradient and a corresponding barotropic meridional pressure gradient at depth. The barotropic pressure gradient drives the zonal barotropic flow, which interacts with the ridge and produces the TFS, i.e., the zonal pressure difference across the ridge. A meridional geostrophic flow (return flow) balanced by TFS compensates for the Ekman transport at the surface, thus slowing and eventually stopping the increase in the surface height gradient leading to the equilibration of the TFS. In this stage, the volume budget is central to the establishment of the vertically integrated zonal momentum balance between wind stress and TFS: the two stresses balance meridional flows at the surface and at depth and are linked by flow continuity rather than the transfer of momentum by stresses throughout the interior. In stage 2 (the following 80 years or so after stage 1), the wind-driven upwelling steepens isopycnals, thereby generating a baroclinic pressure gradient that opposes the barotropic pressure gradient established by the surface height, and thus acts to reduce the return flow. An imbalance between the Ekman transport and return flow at depth, caused by the baroclinicity, leads to a further increase in the sea surface height gradient, maintaining the zonal barotropic flow and thereby TFS. This adjustment, in which the barotropic dynamics compensate for baroclinicity, continues until the wind-driven isopycnal steepening is balanced by the eddy-induced isopycnal flattening. As a result of the eddy-driven isopycnal flattening, there is a vertical redistribution of the geostrophic (thermal wind) shear in the interior by eddies (hence downward EP flux). Our results show that the vertically integrated momentum balance between wind stress and TFS is achieved during the first month (stage 1) and then maintained during the adjustment of the baroclinic structure (stage 2) to equilibrium by the barotropic dynamics.

Our results are generally consistent with previous studies (Johnson and Bryden 1989; Ward and Hogg 2011; Howard et al. 2015; Thompson and Naveira Garabato 2014) in their interpretation of transient baroclinic eddies as transferring the zonal momentum downward throughout the ocean interior via interfacial form stresses (EP flux). This eddy momentum transfer is associated with the redistribution of the zonal geostrophic (thermal wind) shear associated with the sloping isopycnals in the interior and, within the context of the local dynamics framework of Thompson and Naveira Garabato (2014), leads to the barotropization of the ACC in the meander regions. However, our results differ from the interpretation by previous studies (e.g., Johnson and Bryden 1989; Ward and Hogg 2011; Howard et al. 2015) that baroclinic eddies transfer the wind stress from the surface downward to TFS at the bottom. We show that TFS at the bottom is

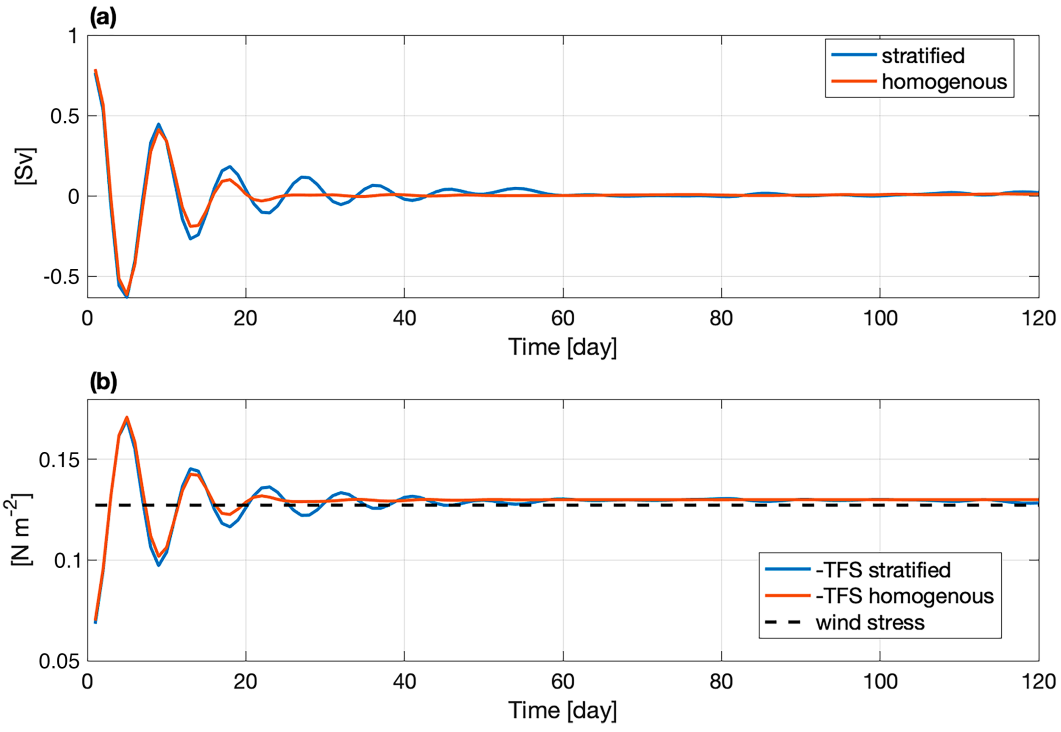

FIG. 12. Time series of (a) meridionally averaged total meridional transport (Sv) and (b) meridionally averaged TFS (N m^{-2}) for the first 4 months following doubling of the wind.

established by barotropic dynamics prior to and independent of the eddy momentum stresses in the interior. Only in the limit of vanishing residual overturning circulation does the rate at which the eddies act to reduce the thermal wind shear by the isopycnal flattening match the rate at which wind generates the thermal wind shear by wind-driven isopycnal steepening in the interior, and hence, EP flux matches wind stress and TFS. However, we show that 1) this adjustment of the isopycnals occurs when the wind–TFS balance is already established and 2) wind stress at the surface and eddies (EP flux) in the interior alone produce no TFS across the ridge unless there is a return flow at depth required by the barotropic (homogeneous) dynamics.

The importance of barotropic dynamics for the ACC meanders has been highlighted in recent studies (e.g., Stewart and Hogg 2017; Youngs et al. 2017; Constantinou and Hogg 2019). A fast response of the wind–TFS balance of the ACC to wind similar to that described here has previously been observed in both a Southern Ocean model (5 days; Masich et al. 2015) and a global coarse-resolution ocean model (1 month; Webb and de Cuevas 2007). A high correlation has also been reported between time series of bottom speed, standing meander curvature, and eddy buoyancy fluxes (Thompson and Naveira Garabato 2014), suggesting barotropic dynamics enable a rapid response of eddy heat fluxes across the ACC to wind perturbations. Previous studies have shown that the eddy heat fluxes are enhanced in regions of standing meanders of the ACC (Abernathey and Cessi 2014; Thompson and Naveira Garabato 2014; Foppert et al. 2017). Abernathey and Cessi (2014) propose a mechanism in which, as standing meanders flex, they increase the local buoyancy gradient, as well as the length of the buoyancy contours, across which eddies carry heat, thereby facilitating the cross-stream heat transport accomplished by transient eddies. In turn, consistent with the results presented here, Zhang et al. (2023) argue that the meander flexing (i.e., changes in its amplitude and curvature) is driven by the bottom (barotropic) flow, which is sensitive to the wind. Combined with the enhancement of eddy fluxes by the meanders (Abernathey and Cessi 2014), the dependence of the meander curvature on the barotropic flow component (Zhang et al. 2023) offers an explanation for the rapid response of the eddy heat fluxes to the wind. Further evidence for the primary role of meanders and barotropic adjustment comes from Kong and Jansen (2022), who report that in flat-bottomed models (without meanders), the residual overturning circulation initially increases with the wind and then is restored by eddies after several decades, while in models with meanders, the residual overturning circulation remains insensitive to the wind, implying a rapid response in eddy buoyancy fluxes.

Acknowledgments. This work was supported in part by funding from the Australian Government as part of the Antarctic Science Collaboration Initiative program, through the Australian Antarctic Program Partnership. This research was undertaken at the NCI National Facility in Canberra, Australia. The authors thank Stephen Griffies and two anonymous reviewers for their constructive comments.

Data availability statement. Datasets analyzed during the current study are available at https://github.com/XihanZh/ACC_momentum_balance.

APPENDIX

Idealized Simulations with Wind Stress and No TFS

We present results from two additional idealized experiments to further show that the wind–TFS balance is controlled by barotropic dynamics. Specifically, the results demonstrate that TFS across the ridge does not develop, regardless of the absence or presence of transient baroclinic eddies, if there is no return flow at depth.

Experiment 1: A doubly periodic domain on an f plane with a meridional ridge in the middle of the domain. The model is forced by a spatially uniform zonal wind stress of 0.1 N m^{-2} at the surface. The flow is stratified with a linear vertical temperature distribution changing from 0°C above the ridge to 8°C at the surface. No surface heat flux and temperature restoring in the northern sponge layer is applied. Other model parameters are the same as in the main experiments described in the methods section. The simulation quickly equilibrates with the surface Ekman layer dynamics and no circulation below it (Fig. A1). The wind stress is balanced within the Ekman layer (and also over the entire depth) by the Coriolis force associated with the meridional Ekman transport. Given that the domain is periodic in the meridional direction, the Ekman transport is unbounded, and thus, there is no return flow at depth—hence, there is no TFS at the ridge. The flow is stratified, but the isopycnals remain flat throughout the whole simulation, i.e., no baroclinic eddies develop. While the wind stress is applied at the surface, TFS is not required at the bottom to achieve a balanced state.

Experiment 2: The same simulation as above but now with the temperature restoring to a meridionally periodic distribution in the interior, which leads to the steepening of isopycnals from their flat distribution in Experiment 1 and the generation of transient baroclinic eddies. At equilibrium, the eddies are fully developed, yet there is no TFS at the bottom and the time-averaged zonal momentum balance remains the same as in Experiment 1 (Fig. A2). While the transient baroclinic eddies are present in this simulation and are characterized by the downward eddy momentum stresses (EP flux) in the interior, they do not transfer wind stress from the surface through to the bottom for it to be balanced by TFS. At equilibrium, there are two opposing thermal wind-driven jets and a fully developed eddy field, and yet there is still no large-scale TFS balancing the uniform wind stress at the surface.

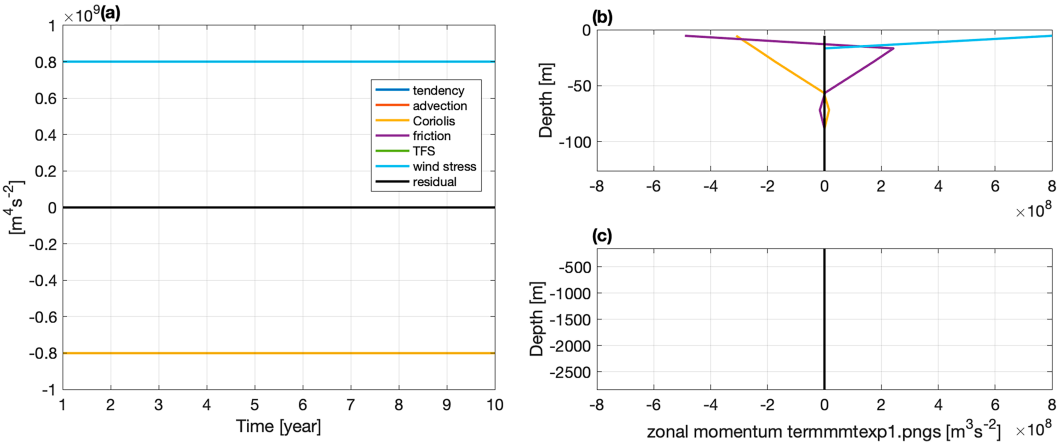

FIG. A1. Experiment 1 results. (a) Time series of the volume integrated zonal momentum balance terms (m^4 s^{-2}). Vertical profiles of the time-mean horizontally integrated zonal momentum balance terms (m^3 s^{-2}) in (b) upper 120 m and (c) entire ocean depth below 120 m.

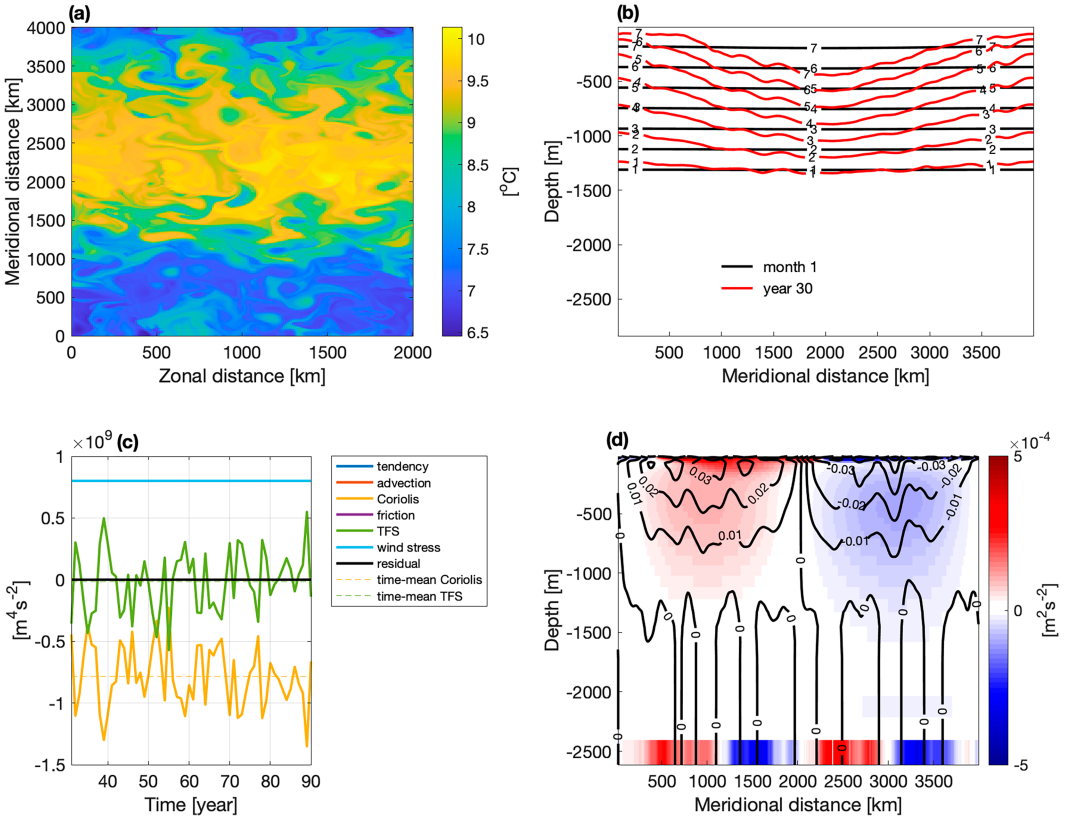

FIG. A2. Experiment 2 results. (a) A snapshot of the sea surface temperature (°C). (b) Zonally averaged temperature distribution (°C) illustrating initial (after 1 month) and final equilibrated isopycnal slopes. (c) Time series of the volume integrated zonal momentum balance terms ($m^4\ s^{-2}$). (d) Time-averaged and zonally averaged vertical component of EP flux ($m^2\ s^{-2}$) and zonal velocity (black contours; $m\ s^{-1}$).

REFERENCES

Abernathey, R., and P. Cessi, 2014: Topographic enhancement of eddy efficiency in baroclinic equilibration. *J. Phys. Oceanogr.*, **44**, 2107–2126, https://doi.org/10.1175/JPO-D-14-0014.1.

——, J. Marshall, and D. Ferreira, 2011: The dependence of Southern Ocean meridional overturning on wind stress. *J. Phys. Oceanogr.*, **41**, 2261–2278, https://doi.org/10.1175/JPO-D-11-023.1.

Allison, L. C., H. L. Johnson, and D. P. Marshall, 2011: Spin-up and adjustment of the Antarctic Circumpolar Current and global pycnocline. *J. Mar. Res.*, **69**, 167–189, https://doi.org/10.1357/002224011798765330.

Andrews, D. G., and M. E. McIntyre, 1976: Planetary waves in horizontal and vertical shear: The generalized Eliassen-Palm relation and the mean zonal acceleration. *J. Atmos. Sci.*, **33**, 2031–2048, https://doi.org/10.1175/1520-0469(1976)033<2031:PWIHAV>2.0.CO;2.

Bai, Y., Y. Wang, and A. L. Stewart, 2021: Does topographic form stress impede prograde ocean currents? *J. Phys. Oceanogr.*, **51**, 2617–2638, https://doi.org/10.1175/JPO-D-20-0189.1.

Constantinou, N. C., and A. M. Hogg, 2019: Eddy saturation of the Southern Ocean: A baroclinic versus barotropic perspective. *Geophys. Res. Lett.*, **46**, 12 202–12 212, https://doi.org/10.1029/2019GL084117.

Döös, K., and D. J. Webb, 1994: The deacon cell and the other meridional cells of the Southern Ocean. *J. Phys. Oceanogr.*, **24**, 429–442, https://doi.org/10.1175/1520-0485(1994)024<0429:TDCATO>2.0.CO;2.

Foppert, A., K. A. Donohue, D. R. Watts, and K. L. Tracey, 2017: Eddy heat flux across the Antarctic Circumpolar Current estimated from sea surface height standard deviation. *J. Geophys. Res. Oceans*, **122**, 6947–6964, https://doi.org/10.1002/2017JC012837.

Gent, P. R., and J. C. Mcwilliams, 1990: Isopycnal mixing in ocean circulation models. *J. Phys. Oceanogr.*, **20**, 150–155, https://doi.org/10.1175/1520-0485(1990)020<0150:IMIOCM>2.0.CO;2.

Howard, E., A. M. Hogg, S. Waterman, and D. P. Marshall, 2015: The injection of zonal momentum by buoyancy forcing in a Southern Ocean model. *J. Phys. Oceanogr.*, **45**, 259–271, https://doi.org/10.1175/JPO-D-14-0098.1.

Ito, T., and J. Marshall, 2008: Control of lower-limb circulation in the Southern Ocean by diapycnal mixing and mesoscale eddy transfer. *J. Phys. Oceanogr.*, **38**, 2832–2845, https://doi.org/10.1175/2008JPO3878.1.

Jackson, L., C. W. Hughes, and R. G. Williams, 2006: Topographic control of basin and channel flows: The role of bottom pressure torques and friction. *J. Phys. Oceanogr.*, **36**, 1786–1805, https://doi.org/10.1175/JPO2936.1.

Johnson, G. C., and H. L. Bryden, 1989: On the size of the Antarctic Circumpolar Current. *Deep-Sea Res.*, **36A**, 39–53, https://doi.org/10.1016/0198-0149(89)90017-4.

Kong, H., and M. F. Jansen, 2022: Time-dependent response of the overturning circulation and pycnocline depth to Southern Ocean surface wind stress changes. *J. Phys. Oceanogr.*, **52**, 759–774, https://doi.org/10.1175/JPO-D-21-0214.1.

Lumpkin, R., and K. Speer, 2007: Global ocean meridional overturning. *J. Phys. Oceanogr.*, **37**, 2550–2562, https://doi.org/10.1175/JPO3130.1.

Marshall, D. P., M. H. P. Ambaum, J. R. Maddison, D. R. Munday, and L. Novak, 2017: Eddy saturation and frictional control of the Antarctic Circumpolar Current. *Geophys. Res. Lett.*, **44**, 286–292, https://doi.org/10.1002/2016GL071702.

Marshall, J., and T. Radko, 2003: Residual-mean solutions for the Antarctic Circumpolar Current and its associated overturning circulation. *J. Phys. Oceanogr.*, **33**, 2341–2354, https://doi.org/10.1175/1520-0485(2003)033<2341:RSFTAC>2.0.CO;2.

——, and ——, 2006: A model of the upper branch of the meridional overturning of the Southern Ocean. *Prog. Oceanogr.*, **70**, 331–345, https://doi.org/10.1016/j.pocean.2006.07.004.

——, D. Olbers, H. Ross, and D. Wolf-Gladrow, 1993: Potential vorticity constraints on the dynamics and hydrography of the Southern Ocean. *J. Phys. Oceanogr.*, **23**, 465–487, https://doi.org/10.1175/1520-0485(1993)023<0465:PVCOTD>2.0.CO;2.

——, A. Adcroft, C. Hill, L. Perelman, and C. Heisey, 1997: A finite-volume, incompressible Navier stokes model for studies of the ocean on parallel computers. *J. Geophys. Res.*, **102**, 5753–5766, https://doi.org/10.1029/96JC02775.

Masich, J., T. K. Chereskin, and M. R. Mazloff, 2015: Topographic form stress in the Southern Ocean state estimate. *J. Geophys. Res. Oceans*, **120**, 7919–7933, https://doi.org/10.1002/2015JC011143.

——, M. R. Mazloff, and T. K. Chereskin, 2018: Interfacial form stress in the Southern Ocean state estimate. *J. Geophys. Res. Oceans*, **123**, 3368–3385, https://doi.org/10.1029/2018JC013844.

Munday, D. R., H. L. Johnson, and D. P. Marshall, 2013: Eddy saturation of equilibrated circumpolar currents. *J. Phys. Oceanogr.*, **43**, 507–532, https://doi.org/10.1175/JPO-D-12-095.1.

——, ——, and ——, 2015: The role of ocean gateways in the dynamics and sensitivity to wind stress of the early Antarctic Circumpolar Current. *Paleoceanogr. Paleoclimatol.*, **30**, 284–302, https://doi.org/10.1002/2014PA002675.

Munk, W. H., and E. Palmén, 1951: Note on the dynamics of the Antarctic Circumpolar Current. *Tellus*, **3A** (1), 53–55, https://doi.org/10.3402/tellusa.v3i1.8609.

Nadeau, L.-P., and R. Ferrari, 2015: The role of closed gyres in setting the zonal transport of the Antarctic Circumpolar Current. *J. Phys. Oceanogr.*, **45**, 1491–1509, https://doi.org/10.1175/JPO-D-14-0173.1.

Naveira Garabato, A. C., A. J. G. Nurser, R. B. Scott, and J. A. Goff, 2013: The impact of small-scale topography on the dynamical balance of the ocean. *J. Phys. Oceanogr.*, **43**, 647–668, https://doi.org/10.1175/JPO-D-12-056.1.

Nikurashin, M., and G. Vallis, 2011: A theory of deep stratification and overturning circulation in the ocean. *J. Phys. Oceanogr.*, **41**, 485–502, https://doi.org/10.1175/2010JPO4529.1.

——, and R. Ferrari, 2013: Overturning circulation driven by breaking internal waves in the deep ocean. *Geophys. Res. Lett.*, **40**, 3133–3137, https://doi.org/10.1002/grl.50542.

Olbers, D., 1998: Comments on "on the obscurantist physics of 'form drag' in theorizing about the circumpolar current. *J. Phys. Oceanogr.*, **28**, 1647–1654, https://doi.org/10.1175/1520-0485(1998)028<1647:COOTOP>2.0.CO;2.

——, D. Borowski, C. Völker, and J.-O. Wöelff, 2004: The dynamical balance, transport and circulation of the Antarctic Circumpolar Current. *Antarct. Sci.*, **16**, 439–470, https://doi.org/10.1017/S0954102004002251.

Patmore, R. D., P. R. Holland, D. R. Munday, A. C. Naveira Garabato, D. P. Stevens, and M. P. Meredith, 2019: Topographic control of Southern Ocean gyres and the Antarctic Circumpolar Current: A barotropic perspective. *J. Phys. Oceanogr.*, **49**, 3221–3244, https://doi.org/10.1175/JPO-D-19-0083.1.

Pedlosky, J., 1996: *Ocean Circulation Theory*. Springer-Verlag, 453 pp.

Rintoul, S. R., C. W. Hughes, and D. Olbers, 2001: The Antarctic Circumpolar Current system. *Ocean Circulation and Climate; Observing and Modelling the Global Ocean*, G. Siedler, J. Church, and J. Gould, Eds., International Geophysics Series, Vol. 77, Academic Press, 271–302.

Stewart, A. L., and A. M. Hogg, 2017: Reshaping the Antarctic Circumpolar Current via Antarctic bottom water export. *J. Phys. Oceanogr.*, **47**, 2577–2601, https://doi.org/10.1175/JPO-D-17-0007.1.

Straub, D. N., 1993: On the transport and angular momentum balance of channel models of the Antarctic Circumpolar Current. *J. Phys. Oceanogr.*, **23**, 776–782, https://doi.org/10.1175/1520-0485(1993)023<0776:OTTAAM>2.0.CO;2.

Thompson, A. F., and A. C. Naveira Garabato, 2014: Equilibration of the Antarctic Circumpolar Current by standing meanders. *J. Phys. Oceanogr.*, **44**, 1811–1828, https://doi.org/10.1175/JPO-D-13-0163.1.

Tréguier, A.-M., and J. C. McWilliams, 1990: Topographic influences on wind-driven, stratified flow in a β-plane channel: An idealized model for the Antarctic Circumpolar Current. *J. Phys. Oceanogr.*, **20**, 321–343, https://doi.org/10.1175/1520-0485(1990)020<0321:TIOWDS>2.0.CO;2.

Vallis, G. K., 2019: *Essentials of Atmospheric and Oceanic Dynamics*. Cambridge University Press, 356 pp.

Ward, M. L., and A. M. Hogg, 2011: Establishment of momentum balance by form stress in a wind-driven channel. *Ocean Modell.*, **40**, 133–146, https://doi.org/10.1016/j.ocemod.2011.08.004.

Webb, D. J., and B. A. de Cuevas, 2007: On the fast response of the Southern Ocean to changes in the zonal wind. *Ocean Sci.*, **3**, 417–427, https://doi.org/10.5194/os-3-417-2007.

Youngs, M. K., and G. R. Flierl, 2023: Extending residual-mean overturning theory to the topographically localized transport in the Southern Ocean. *J. Phys. Oceanogr.*, **53**, 1901–1915, https://doi.org/10.1175/JPO-D-22-0217.1.

——, A. F. Thompson, A. Lazar, and K. J. Richards, 2017: ACC meanders, energy transfer, and mixed barotropic–baroclinic instability. *J. Phys. Oceanogr.*, **47**, 1291–1305, https://doi.org/10.1175/JPO-D-16-0160.1.

Zhang, X., M. Nikurashin, B. Peña-Molino, S. R. Rintoul, and E. Doddridge, 2023: A theory of standing meanders of the Antarctic Circumpolar Current and their response to wind. *J. Phys. Oceanogr.*, **53**, 235–251, https://doi.org/10.1175/JPO-D-22-0086.1.